Raman spectrosopy and phonon dynamics in strained V_2O_3

Wei-Fan Hsu[1], Simon Mellaerts[1], Pia Homm[1], Noriyuki Uchida[2], Mariela Menghini[1,3], Michel Houssa[1,4], Jin Won Seo[5], and Jean-Pierre Locquet[1]

[1]Department of Physics and Astronomy, KU Leuven, Celestijnenlaan 200D, 3001 Leuven, Belgium, [2]National Institute for Advanced Industrial Science and Technology (AIST), Tsukuba, Ibaraki 305-8562, Japan,[3]IMDEA Nanociencia, Calle Faraday 9, E29049 Madrid, Spain, [4]Imec, Kapeldreef 75, 3001 Leuven, Belgium,[5]Department of Materials Engineering, KU Leuven, Kasteelpark Arenberg 44, 3001 Leuven, Belgium*

Transition metal oxides are known to have a strong interplay of many degrees of freedom giving rise to their rich phase diagrams with competing ground states. The Mott material V_2O_3 hosting a room- and low-temperature metal-insulator transition is a great example where electronic, structural and magnetic ordering are the directors at play. By combining first-principle calculations and Raman spectroscopy, we study the phonon dynamics of V_2O_3 to gain further understanding in the interplay of these ordering mechanisms driving the transitions. Raman spectroscopy is performed on a unique series of epitaxial strained 1.5% Cr-doped V_2O_3 thin films, where both paramagnetic insulating, metallicm, as well as intermediate electronic states are stabilized. This leads to a phonon dynamic study covering the full phase diagram of V_2O_3.

I. INTRODUCTION

Vanadium sesquioxide (V_2O_3) is an archetypical strongly correlated electron system that undergoes both an isosymmetric as well as symmetry-breaking metal-insulator transition (MIT), which can be controlled by temperature, doping, pressure and strain [1–5]. At ambient conditions, V_2O_3 is a paramagnetic metal (PM) with a corundum structure ($R\bar{3}c$) which undergoes a Mott MIT to a paramagnetic insulator (PI) upon Cr doping [6–9]. Additionally, below $\sim$ 180 K a low-temperature (LT) MIT occurs towards an antiferromagnetic insulator (AFI) with a monoclinic structure ($C2/c$).

The corundum structure can be considered as honeycomb lattices in the basal ab-plane AB stacked along the c-axis with the V^{3+} ($3d^2$) ions occupying face-sharing octahedra along the c-axis. The octahedral crystal field (CF) splits the $3d$ orbital into a lower triple-degenerate t_{2g} and upper two-fold degenerate e_g^σ orbital levels, with the former splitting further into an a_{1g} singlet pointing along the c axis, and a lower e_g^π doublet in the basal plane by a trigonal distortion. This in combination with the strong on-site Coulomb repulsion gives rise to a mixture of orbital states resulting in its rich phase diagram.

The RT Mott MIT from PM to PI induced by Cr doping has led to the observation of a discontinuous change in crystal volume and c/a ratio while preserving the space-group symmetry [1], as shown in Figure 1. This first-order isosymmetric MIT with a three-orders change in resistivity provides huge oppurtunities for new electronic devices, where the ultimate aim is to stabilize at the PM-PI phase boundary such that an external trigger leads to a maximal resistivity change. Therefore, our approach is to systematically tune the in-plane lattice parameter a, and thus also the c/a ratio, to stabilize both PM, PI as well as intermediate electronic states. By the use of engineered $(Cr_xFe_{1-x})_2O_3$ buffer layers, the in-plane strain can be controlled in a precise and continuous manner, as shown in Figure 1. The details of this strain-engineering and the corresponding induced MIT can be found in [5].
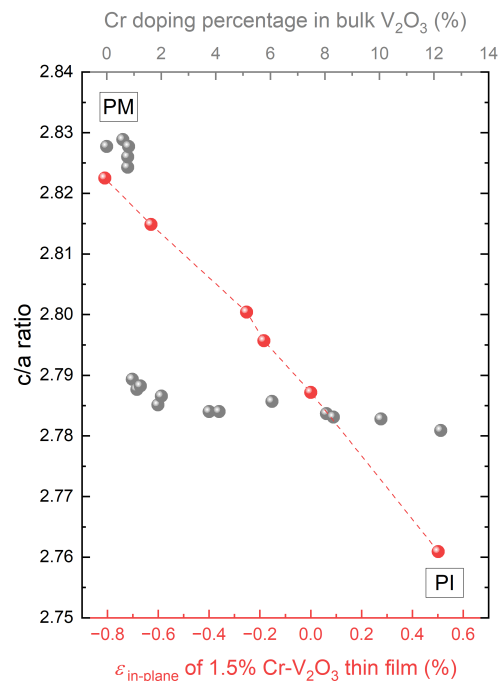

Figure 1. The c/a ratio change in the RT Mott MIT induced by Cr doping in bulk V_2O_3 and by the use of $(Cr_xFe_{1-x})_2O_3$ buffer layers to induce epitaxial strain in 1.5% Cr-doped V_2O_3 thin films. The bulk data was taken from [1].

In this work, we study the dynamics of both the room- and low-temperature MIT of V_2O_3 by a detailed Raman spectroscopy study performed on this unique series of epitaxially strained 1.5% Cr-doped V_2O_3 thin films stabilized in either PM, PI or an intermediate state. In addition, first-principle calculations provide a first complete analysis on the phonon modes of V_2O_3, which facilitates the interpretation of the observed frequency dependences. By the epitaxial stabilization of these 1.5% Cr-doped V_2O_3 thin films, the dynamics of the room-temperature (RT) PM-PI MIT is studied, as well as, the LT PM-AFI and PI-AFI transitions. We show that the Raman active vibrations match the structural distortions occurring within the phase diagram of V_2O_3, which can therefore be used to study the dynamics of the MIT. Moreover, we have evaluated the effect of strain on the LT MIT where there is a gradual change in the dynamics upon epitaxially stabilizing either the PM or PI phase.

II. METHODS

To obtain the PM and PI structure, 60 nm of 1.5% Cr-doped V_2O_3 were grown on different corundum structure templates. The different corundum structures were achieved by varying the composition ratio of $(Cr_xFe_{1-x})_2O_3$ buffer layer on c-plane sapphire (Al_2O_3) substrates. More thin film growth details can be found in our previous work [5].

In-situ reflection high energy electron diffraction (RHEED) was used qualitatively to confirm the epitaxy in each step of the process. After deposition, the samples were characterized by means of high resolution X-ray diffraction (XRD), reflectivity (XRR), and reciprocal space mapping (RSM) using a Panalytical X'pert Pro diffractometer. Raman spectra have been acquired in a Raman microscope (Renishaw, UK) using unpolarized laser excitation with a wavelength of 488 nm and a power of 1.9 mW. The 2 μm diameter spot of the excitation laser is focused on the sample through an objective lens with ×50 magnification while the sample is kept in a vacuum environment at different temperatures. The sample temperature is controlled in the $80\,K - 330\,K$ range by using a micro-heater and a gas flow of liquid N_2 as cooling source.

All first-principle calculations were performed within density functional theory (DFT) as implemented in the Vienna *ab initio* simulation package (VASP) [10]. The interactions between electrons and ions were described by the projector augmented wave (PAW) potentials [11], with the semicore states treated as valence states, V $(3p^63d^44s^1)$. The electronic wave functions were expanded with a cutoff energy of 600 eV, and the PBE functional was used. For the structural relaxation, a force convergence criterion of 0.001 eV/Å was used with the Brillouin zone (BZ) sampled by a $12 \times 12 \times 12$ Γ-centered k-mesh. Phonon dispersions and dielectric properties were calculated self-consistently on the basis of

both the finite displacement method and density functional perturbation theory (DFPT) and with the use of the PHONOPY package [12]. For the self-consistent electronic properties a denser $18\times18\times18$ mesh was used with energy convergence criterion of 10^{-6} eV. The paramagnetic V_2O_3 phases are well-known to be a magnetically frustrated state [13, 14], which makes a non-magnetic approximation inaccurate, while recent studies have shown that the spin-polarized calculations with ferromagnetic (FM) ordering are a proper approximation for the structural components [15, 16].

III. RESULTS

A. Phonon dynamics of V_2O_3

The phonon modes of both the corundum and monoclinic structure have been calculated by DFPT. This study provides a first complete identification of all phonon modes, and their corresponding eigenvector and -frequency, for both the PM and AFI phases. Room-temperature V_2O_3 adopts a corundum structure with spacegroup $R\bar{3}c$ and point group $\bar{3}m$, with 10 atoms per unit cell and thus $3N = 30$ degrees of freedom corresponding to zone-center modes, of which 3 are simple translations (acoustic), while the remaining 27 are optical vibration modes. By group theory analysis, the $\bar{3}m$ point group at Γ has the irreducible representation (normal modes):

$$\Gamma_c = 2A_{1g} + 2A_{1u} + 3A_{2g} + 2A_{2u} + 5E_g + 4E_u,$$

where A_{1g} and E_g are Raman active modes (7), A_{2u} and E_u are infrared (IR) active modes (6), and A_{1u} and A_{2g} are silent modes (5). The corresponding calculated eigenfrequencies of the Raman active modes were derived from the calculated phonon spectrum (see Fig. 2b) and are summarized in Table I (the frequencies of the other phonon modes can be found in the Supplemental Material). Surprisingly, many of the calculated frequencies are relatively close to the experimental value within this spin-polarized PBE approximation and without the need of a Hubbard correction U.

Table I. Raman active phonon modes comparison of the high-temperature corundum structure. The experimental (Exp) data originates from bulk V_2O_3 [17].

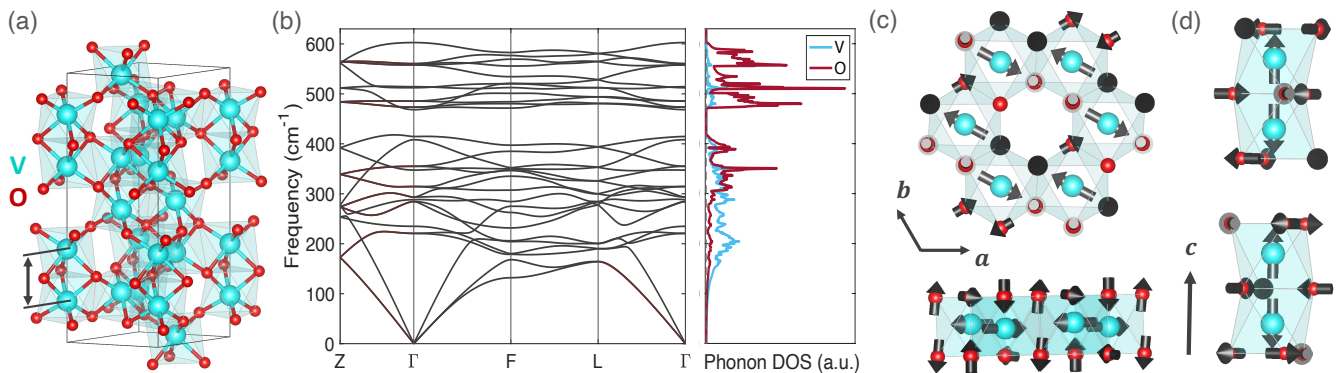| Mode	Theory (cm^{-1})	Exp. (cm^{-1})
$E_g(1)$	221	210
$A_{1g}(1)$	288	234
$E_g(2)$	293	296
$E_g(3)$	314	327
$E_g(4)$	473	/
$A_{1g}(2)$	512	501
$E_g(5)$	560	595

Figure 2. Crystal structure and atomic-resolved phonon dynamics of room-temperature V$_2$O$_3$. (a) The conventional corundum unit cell with the marked short V-V bond. (b) The calculated phonon spectrum projected on a rhombohedral Brillouin zone path and the corresponding phonon density of states. (c) An upper and side view of the $E_g(1)$ mode. (d) A side view of the $A_{1g}(1)$ mode. Note that the eigenvectors are not scaled, the amplitude of the oxygen eigenvectors has been increased to make their motion visible. Cyan and red atoms correspond to vanadium and oxygen, respectively.

Table II. Calculated Raman mode frequencies of the low-temperature monoclinic structure compared to their experimental value. Note that the experimental vibration mode at 233 cm^{-1} is marked with asterisk to indicate it either belongs to $B_g(1)$ or $B_g(2)$.

PM mode	AFI mode	Theory (cm^{-1})	Exp. (cm^{-1}) [80K]	PM mode	AFI mode	Theory (cm^{-1})	Exp. (cm^{-1}) [80K]
$E_g(1)$	$A_g(1)$	157	192	$A_{2g}(2)$	$B_g(5)$	382	/
	$B_g(1)$	183	233*	$E_g(4)$	$A_g(5)$	454	/
$A_{2g}(1)$	$B_g(2)$	200	233*		$B_g(6)$	457	/
$A_{1g}(1)$	$A_g(2)$	256	280	$A_{1g}(2)$	$A_g(6)$	493	525
$E_g(2)$	$B_g(3)$	266	290	$E_g(5)$	$A_g(7)$	545	552
	$A_g(3)$	281	/		$B_g(7)$	546	/
$E_g(3)$	$B_g(4)$	291	325	$A_{2g}(3)$	$B_g(8)$	589	664
	$A_g(4)$	312	340				

Note that the two-fold degenerate E_g modes are in-plane vibrations that lower the symmetry from $\bar{3}m$ to $2/m$, making the AB-stacked hexagons asymmetric, while the antisymmetric A_{1g} modes are out-of-plane vibrations along the c-axis that corresponds to a breathing mode in which there is a shortening/elongation of the shortest V-V bond (see Figure 2c-d). Moreover, these E_g modes at different frequencies are all very similar in their vibrational nature with the main difference in their oxygen movement. From the phonon density of states (DOS), shown in Figure 2b, it can be seen that the low-frequency phonon modes are dominated by the V cation motion, while for the higher frequency modes the vibrations consist of strong oxygen movements. For the remainder of this section, we shall focus on the two low-frequency $E_g(1)$ and $A_{1g}(1)$ Raman modes and their effect on the electronic properties.

Interestingly, these Raman active vibrations also relate to the structural changes that occur upon phase transition from PM towards PI and AFI. In the isosymmetric Mott transition from PM to PI an increasing V-V bond drives this first-order MIT. In a simplified picture, this is often considered as follows. Upon pressure [2], Cr doping [6–9], or epitaxial strain [5], the shortest V-V bond is shortened (with reduced c/a ratio) which causes an increased a_{1g} orbital overlap and triggers the strong on-site Coulomb repulsions causing the elongation of the bond. This cation movement has two main effects opening an energy gap; it decreases the a_{1g} occupation [18] while simultaneously enhancing the trigonal distortion [19]. Therefore probing the A_{1g} mode provides insight on how the V-V bond is altered upon transition. To evaluate the effect of this A_{1g} vibration on the electronic structure, the eigenvector displacement was applied to the relaxed structure of which the DOS was calculated. These calculations confirm that the main changes are caused in the a_{1g} orbital overlap and the CF splitting between a_{1g} and e_g^π (see Supplemental Material). Based on these drastic changes induced in the low-energy electronic bands, it can be inferred that these A_{1g} vibrations will have relatively strong Raman polarizabilities.

Recent ultrafast spectroscopic studies have also shed light on the dynamics of the MIT from PM to AFI [20–22], confirming the existence of an intermediate non-equilibrium photoinduced monoclinic metallic phase [23, 24]. This has led to the identification of two independent structural changes within this phase transition. Upon temperature lowering, the AB stacked hexagons undergo an asymmetric in-plane symmetry-breaking dis-

tortion, similar to the cation movement in the E_g mode, followed by an isosymmetric out-of-plane tilting and elongation of the V-V dimer. Notice that the former movement originates from the inherent magnetic frustration within the hexagons [13, 14], while the latter isosymmetric movement is *a priori* responsible for the first-order nature of this low-temperature MIT, as deduced from Christy's work [25]. Hence, similarly to the A_{1g}, the E_g mode can be used to probe the symmetry-breaking component that drives this LT MIT. Subsequently, the DOS was evaluated for the structure upon E_g displacement, which clearly shows that the two-fold degeneracy of the e_g^π orbital level is lifted (see Supplemental Material) by the broken hexagonal symmetry.

On the other hand, the low-temperature V_2O_3 phase has a monoclinic $C2/c$ structure with point group $2/m$ and irreducible representation:

$$\Gamma_m = 7A_g + 6A_u + 8B_g + 6B_u$$

where A_g, B_g are Raman active (15), and A_u, B_u are IR active (12). Hence, by lowering the three-fold symmetry, the two-fold degenerate E_g modes in the high-symmetric corundum structure are split in a B_g and A_g mode, which are respectively symmetric and antisymmetric with respect to the tilted two-fold rotation axis in the monoclinic structure. On the other hand, the A_{1g} mode loses its vertical mirror symmetry plane and becomes a A_g mode in the monoclinic structure. Additionally, the three silent A_{2g} of the corundum phase transform into Raman active B_g modes. To study the effect of the antiferromagnetic (AF) ordering on the dynamics, the phonon spectra were calculated by a finite displacement method where both spin-polarized FM (approximating paramagnetic ordering) and AF orderings are imposed (see Supplemental Material). The resulting phonon spectrum and corresponding DOS with AF ordering is shown in Figure 3. The derived Raman mode frequencies are also compared to their experimental value, as shown in Table II. It is clear that there is an overall underestimation of the phonon frequency.

B. Epitaxially strained V_2O_3

A unique series of 1.5% Cr-doped V_2O_3 thin films were deposited on $(Cr_xFe_{1-x})_2O_3$ buffer layer with systematically varying the in-plane strain by a precise control of the Fe percentage in the buffer. In this way, the c/a lattice parameter ratio could be controlled in a continuous manner, and thus a transition from PM to PI could be induced as shown in our previous work [5]. Moreover, by transport measurements, intermediate room-temperature resistivity (RTR) states are found to be stabilized (pinned) by this epitaxial strain, as shown in Figure 5.
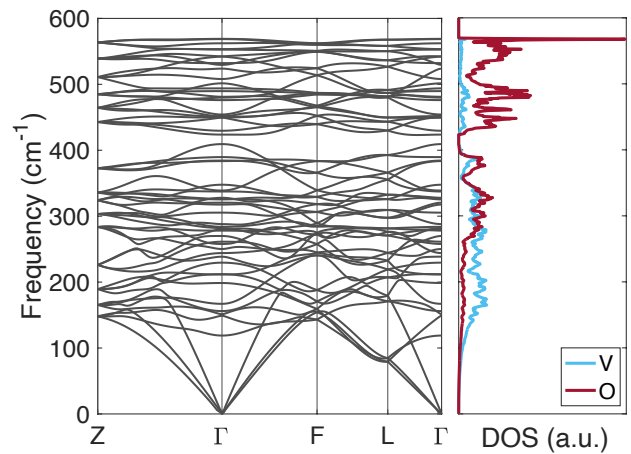

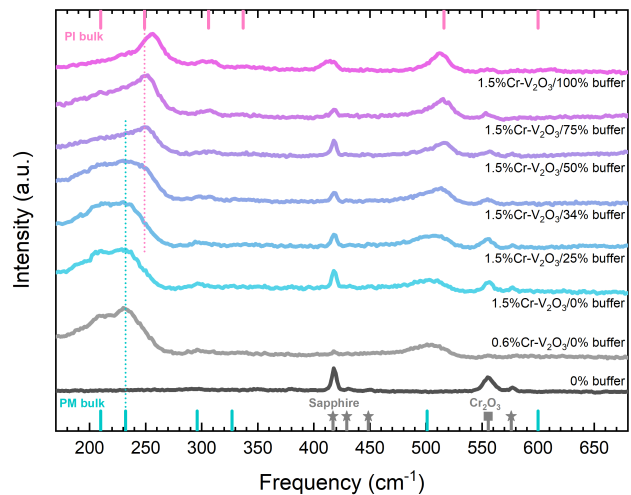Figure 3. DFPT calculated phonon spectrum and corresponding phonon DOS of low-temperature monoclinic AFI V_2O_3.

Figure 4. Room-temperature Raman spectra comparison of 1.5% Cr-doped V_2O_3 thin films upon applying epitaxial strain through different buffer layers. The 0.6% Cr-doped V_2O_3/Cr_2O_3/sapphire is included as a reference of a pure and relaxed case of V_2O_3 thin film. The Raman spectra of Cr_2O_3 thin film on sapphire (with rescaled intensity) is included to show the Raman peaks originating from Cr_2O_3 (square) and sapphire (star).

To study the dynamics of this epitaxially-induced MIT, a comparison of the room-temperature Raman spectra of these strained states is shown in Figure 4. First, it is clear that the A_{1g} modes are much more intense in comparison to the E_g, which was also observed in previous studies [17, 26, 27]. This difference in Raman polarizability can simply be understood by the electronic coupling of these two types of phonon vibrations. From Wannier function calculations, it was shown that the a_{1g} orbital overlap of the $\sigma-$bond along c is much larger compared to the e_g^π orbital overlap of the $\pi-$bonds in the basal plane [28]. Therefore the induced change in orbital po-

larization by the A_{1g} vibrations altering the $\sigma-$ bond will be more pronounced compared to polarizations induced by the E_g vibrations altering the e_g^π orbital overlap. Secondly, a blue shift is observed for each of the Raman active modes (both A_{1g} and E_g modes), which is expected upon transition from PM to PI [17]. Note that this frequency stiffening of the optical phonon modes is in contrast to the softening of the acoustic modes upon transition to PI [29].
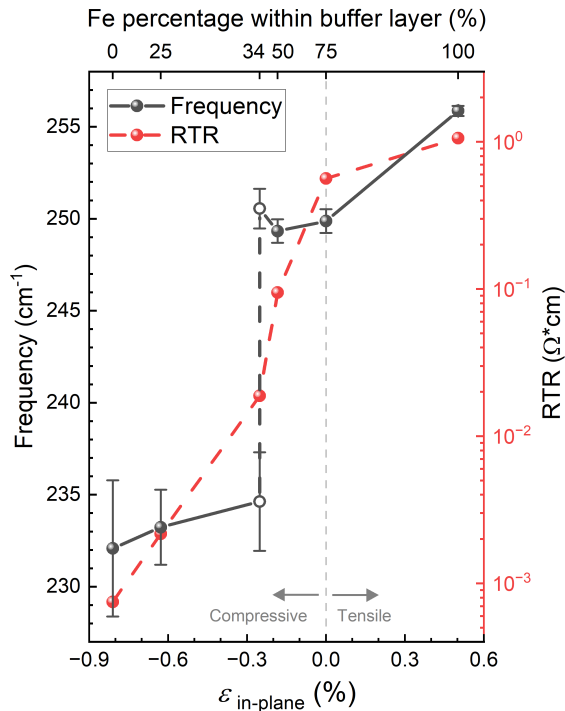

Figure 5. Frequency of $A_{1g}(1)$ mode of 1.5% Cr-doped V_2O_3 thin film under different strain levels. Room-temperature resistivity (RTR) are plotted in the same range as well to compare to the trend with $A_{1g}(1)$ frequency. Bulk PI lattice parameter is defined as 0.0% as a reference for the different in-plane strain. Note that for the $A_{1g}(1)$ frequency of the sample with 34% Fe buffer layer two empty data points are used to indicate the two deconvoluted peaks inferred from Figure 4, corresponding to PM and PI.

Based on the discussion in Sec. III A, a detailed quantitative analysis (see Supplemental Material) was performed for the out-of-plane $A_{1g}(1)$ mode. The frequency of the $A_{1g}(1)$ mode is shown in Figure 5 as a function of in-plane strain, which was derived from RSM [5]. First, a discontinuous frequency stiffening of $A_{1g}(1)$ mode is observed upon increasing in-plane lattice constant (reduced c/a ratio). This is in contrast to recent Raman studies upon reduced lattice constant (increased c/a ratio) where there is a continuous frequency stiffening of the $A_{1g}(1)$ [27]. Taken into account the vibrational nature of $A_{1g}(1)$, it is expected that this discontinuity relates to a discontinuous change in the $\sigma-$overlap of the a_{1g} orbitals

along the c-axis, or thus simply in the bond length. Indeed, the induced stiffening of $A_{1g}(1)$ upon increasing c/a ratio, as reported by Hu *et al.* [27], is the result of the increased c lattice constant that leads to a continuous elongation of the V-V bond. While upon reduced c/a ratio, a reduced V-V bond length would be expected, however, this leads to a critical a_{1g} orbital occupation that triggers an electron repulsive driven elongation of this dimer. This bandwidth controlled cation movement (in the Mott transition) is discontinuous [30–32], implying the abrupt stiffening of $A_{1g}(1)$ upon epitaxial strain. A very similar abrupt frequency change of the A_{1g} has been observed in the temperature-induced Mott MIT of Ti_2O_3 [33], which is also driven by a changing a_{1g} occupation in its c-axis dimer [34].

Second, note that the thin film at $\varepsilon = -0.25\%$ (34%-Fe buffer layer) has a very broad $A_{1g}(1)$ peak (see Fig. 4), which can be considered as the convolution of two clear distinguishable peaks (see Fig. 5). Hence, this suggests an intermediate phase with coexistence of PM and PI domains. Although such a mixed phase has also been observed in bulk V_2O_3 by scanning photoemission microscopy [35], it remains unclear whether this is happening at an atomic (sub-nanometer) scale or nanometer scale.

Lastly, it can be inferred that the A_{1g} mode shows an asymmetric shape which can be related to a Lorentz-Fano resonance, which means a strong coupling to the electron continuum [36]. This could be anticipated from the fact that A_{1g} will alter the electron occupation of the a_{1g}-derived conduction band. In this respect, it is evident that the asymmetry of the A_{1g} mode reduces upon transition to the PI phase, as seen in Fig. 4.

C. The low-temperature phase transition

As an archetypal Mott insulator material, V_2O_3 undergoes a MIT around 180 K which is accompanied by a change in crystal and magnetic structure. To investigate this LT transition, temperature-dependent Raman spectrum were obtained for 0.6% Cr-doped V_2O_3 on a Cr_2O_3 buffer layer, as shown in Figure 6. By the use of our first-principle calculations in Sec. III A, all observed Raman modes have been assigned correctly according to their symmetry. Moreover, a Raman peak observed in the high-frequency region close to 670 cm^{-1} whose origin has remained unidentified in previous work [17] can now be ascribed to a Raman active B_g mode originating from the silent A_{2g} mode in the PM phase.

To study the dynamics of the LT MIT, the frequency changes of the Raman modes are studied in more detail. It is observed that the Raman active vibrations of the PM phase transit into the AFI modes with a transformation of the A_{1g} into a lower symmetry A_g mode, while the two-fold degenerate E_g splits into (A_g, B_g) upon symmetry reduction to the monoclinic AFI phase. Interestingly,
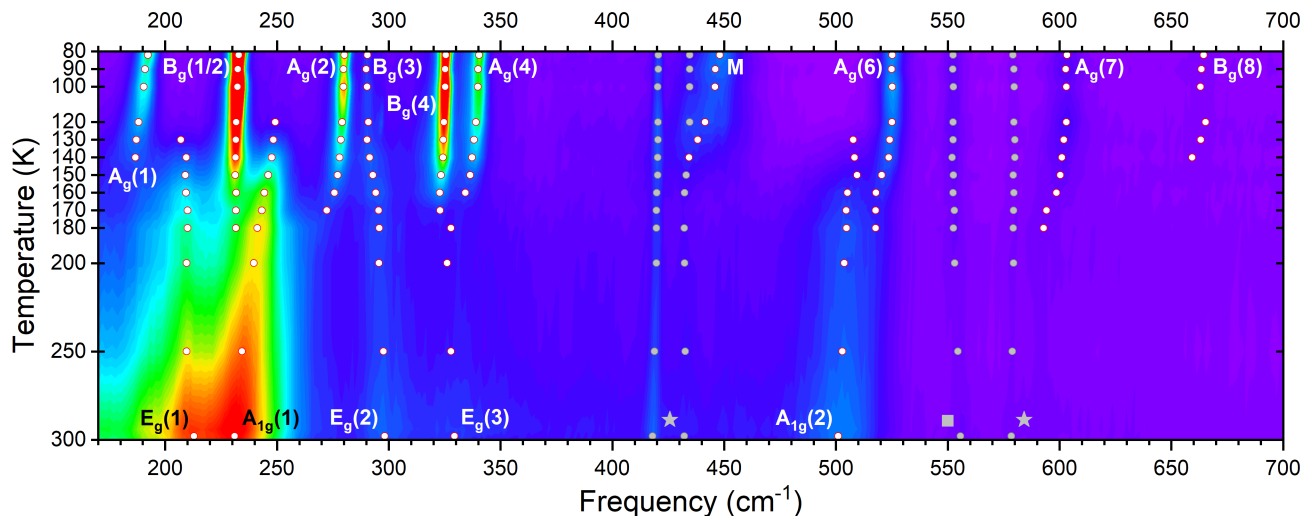
Figure 6. Temperature-dependent Raman spectrum of 0.6% Cr-doped V_2O_3/Cr_2O_3/sapphire. Frequency labeled by star and square represent the peaks from sapphire substrate and Cr_2O_3 buffer layer, respectively. The intensity of the spectrum is plotted in logarithmic scale. Moreover, data in between the dots is interpolated by the software.

these lower-symmetry AFI modes already occur around 180 K, while the PM modes remain up to ~ 120 K, implying there is a phase coexistence within a temperature range of $120 - 180$ K, characteristic to a first-order transition, and also observed earlier [37]. From the HT side, lowering the temperature from PM towards the AFI phase boundary, results in a stiffening of the out-of-plane A_{1g} modes, and the softening of the in-plane E_g modes. On the other hand, considering the AFI upon temperature increase, all Raman modes show a frequency softening towards the transition temperature T_c, including the two A_g modes corresponding to the A_{1g} of the HT phase.

Firstly, the frequency stiffening upon transition from A_{1g} to A_g suggests the elongation of the V-V dimer along the c-axis, as discussed in the Sec. III A. Moreover, this occurs discontinuously, similar to the strain-induced PM-PI transition in Sec. III C, which implies that a similar bandwidth-controlled-driven cation motion is dictating this isosymmetric part of the structural MIT.

Secondly, the frequency softening of almost all AFI Raman active modes show a functional behavior which is characterstic for soft-mode ferroelectric phase transitions. Cochran showed that the soft phonon mode frequency (ω_s) can be considered as an order parameter in these displacive phase transitions with temperature dependence $\omega_s^2 \sim (T - T_c)^{-1}$, where T_c is the transition temperature [38]. While Bismayer showed that this concept could be generalized to hard phonon modes at higher frequencies [39]. Figure 7 shows the frequency dependence of $A_g(2)$, $A_g(7)$ and the magnon mode with their corresponding Cochran law fit (other modes can be found in the Supplementary Material). This behavior confirms the displacive nature of this LT MIT and is also in agreement with previous studies which hypothesized

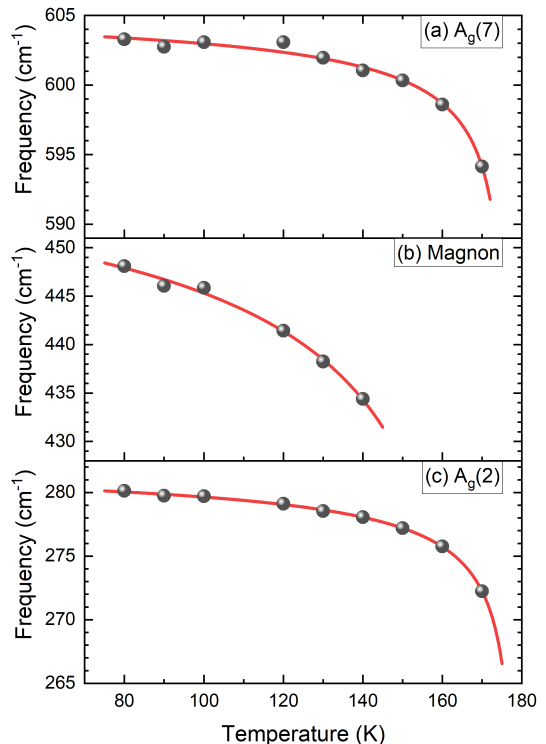the martensitic nature of this LT MIT [21, 40].

Figure 7. Experimental temperature dependence and Cochran law fit of (a) $A_g(7)$, (b) Magnon, and (c)$A_g(2)$.

Finally, upon transition to the AFI phase, a magnon mode (M) can be observed at ~ 450 cm^{-1}. This magnon excitation has been ascribed to a spin wave in the basal ab -plane [41], which emerges by the broken hexagonal symmetry in the AFI phase [14]. This magnon mode

also follows Cochran's law (Curie-Bloch law), as can be seen in Figure 7b.

D. The effect of strain on the low-temperature transition

By the lattice mismatch induced strain, both PM and PI as well as intermediate RTR states are epitaxially stabilized. Although electronically different at room-temperature, the questions arise (1) whether these states differ in their LT AFI phase, and (2) how the dynamics of the LT transition change with epitaxial strain.

To answer the first question, the Raman spectra of each strained thin film were taken at 80 K, as shown in Figure 8. It can be seen that the overall Raman spectra are very similar, with negligible frequency shifts in the modes (see also Supplemental Material), which would imply minor effect of the strain on the AFI structure. This is in agreement with previous optical and transport measurements, which show a convergence to equivalent resistivity values upon temperature reduction [5]. Taking into account that the electrical resistivity highly depends on the V-V bond length, it can be concluded that this bond length is almost unaffected in the AFI by the applied strain.
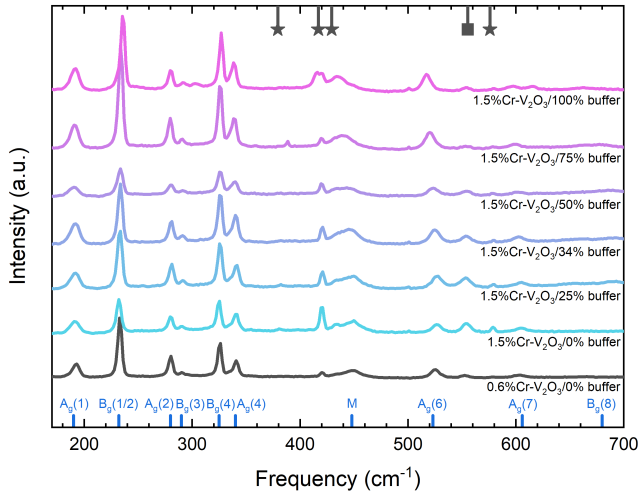

Figure 8. Low-temperature Raman spectra of 1.5% Cr-doped V_2O_3 thin films upon epitaxial strain comparison at 80 K. The vibration modes contributions from sapphire and Cr_2O_3 buffer layer are labeled as star and square, respectively.

Subsequently, the effect on the magnetic structure is evaluated by analyzing the frequency change of the magnon mode in the AFI upon strain (shown in the Supplemental Material). It is observed that the magnon mode softens upon increasing lattice constant (towards PI phase at RT), which was also shown in neutron scattering studies [13]. This relates to the magnetic correlations being shorter ranged in the insulating phase [14, 42].

Previous studies have shown that the LT MIT becomes more continuous upon Cr doping, i.e. for a transition
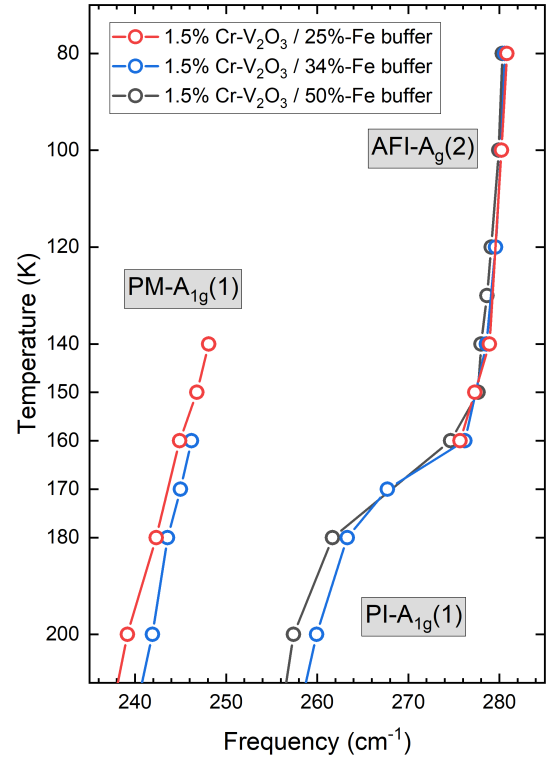

Figure 9. Low-temperature phase transition of 1.5% Cr-doped V_2O_3 under different strain levels. The phase transition change from PM-to-AFI and PI-to-AFI transition by increasing Fe percentage in the buffer layer.

from PI to AFI [29]. Hence, a similar behavior can be expected for increasing lattice constant (increasing Fe percentage in the buffer layer) in the 1.5% Cr-doped V_2O_3 thin films. Upon consideration of the discussion in Sec. III A, the main difference between the PM and PI resides in the V-V bond length and therefore also their difference in MIT dynamics. In this respect, it has been chosen to study the $A_{1g}(1) \rightarrow A(2)$ as a function of temperature to assess the effect of strain on the LT MIT dynamics, demonstrated in Figure 9. For the PM phase (1.5% Cr-doped V_2O_3 on 25%-Fe buffer layer), there is a strongly discontinuous change from $A_{1g}(1)$ to $A_g(2)$ with a coexistence of both peaks in the temperature region between 140 K and 150 K, characteristic to its first-order nature. However, for the PI phase (1.5% Cr-doped V_2O_3 on 50%-Fe buffer layer), the $A_{1g}(1)$ is shifted to higher frequencies as the temperature decreases, resulting in a continuous transition into the lower-symmetry $A_g(2)$ mode. Additionally, the mixed phase on 34%-Fe buffer layer showing both PM and PI $A_{1g}(1)$ mode with respectively an abrupt and continuous transition to AFI-$A_g(2)$. These results suggest that the LT transition becomes continuous is related to the elongated V-V bond length, or, thus, the absence of the isosymmetric elongation of the V-V dimer in the structural transition.

IV. CONCLUSIONS

The present results combining first-principle methods and Raman spectroscopy on this unique set of strained 1.5% Cr-doped V_2O_3 thin films sheds light on the dynamics upon the PM-PI, PM-AFI and PI-AFI transitions. The first-principle calculations have provided a first complete identification and symmetry assignment of all phonon modes of PM and AFI V_2O_3. Moreover, they have shown that the Raman active vibrations relate to the structural distortions that drive the RT and LT transitions, and can be used to probe their dynamics. In this way, we prove that the RT isosymmetric Mott MIT is driven by a local first-order V-V dimer elongation. On the other hand, we explicitly identify the displacive nature of the LT MIT by hard phonon mode spectroscopy analysis [39]. Finally, we confirm that the LT transition becomes continuous as the RT phase of V_2O_3 becomes more insulating. This phenomenon can solely be ascribed to the elongated V-V bond length in the PI phase, while the isosymmetric V-V dimer elongation is fundamental to the first-order nature of the LT MIT.

[1] D. B. McWhan and J. P. Remeika, Phys. Rev. B **2**, 3734 (1970).

[2] D. B. McWhan, T. M. Rice, and J. P. Remeika, Phys. Rev. Lett. **23**, 1384 (1969).

[3] F. Rodolakis, P. Hansmann, J.-P. Rueff, A. Toschi, M. W. Haverkort, G. Sangiovanni, A. Tanaka, T. Saha-Dasgupta, O. K. Andersen, K. Held, M. Sikora, I. Alliot, J.-P. Itié, F. Baudelet, P. Wzietek, P. Metcalf, and M. Marsi, Phys. Rev. Lett. **104**, 047401 (2010).

[4] P. Homm, L. Dillemans, M. Menghini, B. Van Bilzen, P. Bakalov, C.-Y. Su, R. Lieten, M. Houssa, D. Nasr Esfahani, L. Covaci, F. M. Peeters, J. W. Seo, and J.-P. Locquet, Applied Physics Letters **107**, 111904 (2015), https://doi.org/10.1063/1.4931372.

[5] P. Homm, M. Menghini, J. W. Seo, S. Peters, and J. P. Locquet, APL Materials **9**, 021116 (2021), https://doi.org/10.1063/5.0035865.

[6] S. Chen, J. E. Hahn, C. E. Rice, and W. R. Robinson, Journal of Solid State Chemistry **44**, 192 (1982).

[7] A. I. Frenkel, D. M. Pease, J. I. Budnick, P. Metcalf, E. A. Stern, P. Shanthakumar, and T. Huang, Phys. Rev. Lett. **97**, 195502 (2006).

[8] D. Grieger and F. Lechermann, Phys. Rev. B **90**, 115115 (2014).

[9] F. Lechermann, N. Bernstein, I. I. Mazin, and R. Valentí, Phys. Rev. Lett. **121**, 106401 (2018).

[10] G. Kresse and J. Furthmüller, Phys. Rev. B **54**, 11169 (1996).

[11] G. Kresse and D. Joubert, Phys. Rev. B **59**, 1758 (1999).

[12] A. Togo and I. Tanaka, Scr. Mater. **108**, 1 (2015).

[13] W. Bao, C. Broholm, G. Aeppli, S. A. Carter, P. Dai, T. F. Rosenbaum, J. M. Honig, P. Metcalf, and S. F. Trevino, Phys. Rev. B **58**, 12727 (1998).

[14] J. C. Leiner, H. O. Jeschke, R. Valentí, S. Zhang, A. T. Savici, J. Y. Y. Lin, M. B. Stone, M. D. Lumsden, J. Hong, O. Delaire, W. Bao, and C. L. Broholm, Phys. Rev. X **9**, 011035 (2019).

[15] D. Wickramaratne, N. Bernstein, and I. I. Mazin, Phys. Rev. B **99**, 214103 (2019).

[16] D. Wickramaratne, N. Bernstein, and I. I. Mazin, Phys. Rev. B **100**, 205204 (2019).

[17] C. Tatsuyama and H. Y. Fan, Phys. Rev. B **21**, 2977 (1980).

[18] J.-H. Park, L. H. Tjeng, A. Tanaka, J. W. Allen, C. T. Chen, P. Metcalf, J. M. Honig, F. M. F. de Groot, and G. A. Sawatzky, Phys. Rev. B **61**, 11506 (2000).

[19] A. I. Poteryaev, J. M. Tomczak, S. Biermann, A. Georges, A. I. Lichtenstein, A. N. Rubtsov, T. Saha-Dasgupta, and O. K. Andersen, Phys. Rev. B **76**, 085127 (2007).

[20] A. Singer, J. G. Ramirez, I. Valmianski, D. Cela, N. Hua, R. Kukreja, J. Wingert, O. Kovalchuk, J. M. Glownia, M. Sikorski, M. Chollet, M. Holt, I. K. Schuller, and O. G. Shpyrko, Phys. Rev. Lett. **120**, 207601 (2018).

[21] A. Ronchi, P. Homm, M. Menghini, P. Franceschini, F. Maccherozzi, F. Banfi, G. Ferrini, F. Cilento, F. Parmigiani, S. S. Dhesi, M. Fabrizio, J.-P. Locquet, and C. Giannetti, Phys. Rev. B **100**, 075111 (2019).

[22] A. Ronchi, P. Franceschini, A. De Poli, P. Homm, A. Fitzpatrick, F. Maccherozzi, G. Ferrini, F. Banfi, S. S. Dhesi, M. Menghini, M. Fabrizio, J.-P. Locquet, and C. Giannetti, Nature Communications **13**, 3730 (2022).

[23] P. Pfalzer, G. Obermeier, M. Klemm, S. Horn, and M. L. denBoer, Phys. Rev. B **73**, 144106 (2006).

[24] Y. Kalcheim, N. Butakov, N. M. Vargas, M.-H. Lee, J. del Valle, J. Trastoy, P. Salev, J. Schuller, and I. K. Schuller, Phys. Rev. Lett. **122**, 057601 (2019).

[25] A. G. Christy, Acta Crystallographica Section B **51**, 753 (1995).

[26] N. Kuroda and H. Y. Fan, Phys. Rev. B **16**, 5003 (1977).

[27] L. Hu, C. Xie, S. J. Zhu, M. Zhu, R. H. Wei, X. W. Tang, W. J. Lu, W. H. Song, J. M. Dai, R. R. Zhang,

C. J. Zhang, X. B. Zhu, and Y. P. Sun, Phys. Rev. B **103**, 085119 (2021).

[28] I. S. Elfimov, T. Saha-Dasgupta, and M. A. Korotin, Phys. Rev. B **68**, 113105 (2003).

[29] M. Yethiraj, S. A. Werner, W. B. Yelon, and J. M. Honig, Phys. Rev. B **36**, 8675 (1987).

[30] N. F. Mott, Canadian Journal of Physics **34**, 1356 (1956), https://doi.org/10.1139/p56-151.

[31] M. Imada, A. Fujimori, and Y. Tokura, Rev. Mod. Phys. **70**, 1039 (1998).

[32] S. Mellaerts, J. W. Seo, V. Afanas'ev, M. Houssa, and J.-P. Locquet, Phys. Rev. Materials **6**, 064410 (2022).

[33] S. H. Shin, R. L. Aggarwal, B. Lax, and J. M. Honig, Phys. Rev. B **9**, 583 (1974).

[34] C. F. Chang, T. C. Koethe, Z. Hu, J. Weinen, S. Agrestini, L. Zhao, J. Gegner, H. Ott, G. Panaccione, H. Wu, M. W. Haverkort, H. Roth, A. C. Komarek, F. Offi, G. Monaco, Y.-F. Liao, K.-D. Tsuei, H.-J. Lin, C. T. Chen, A. Tanaka, and L. H. Tjeng, Phys. Rev. X **8**, 021004 (2018).

[35] S. Lupi, L. Baldassarre, B. Mansart, A. Perucchi, A. Barinov, P. Dudin, E. Papalazarou, F. Rodolakis, J. P. Rueff, J. P. Itié, S. Ravy, D. Nicoletti, P. Postorino, P. Hansmann, N. Parragh, A. Toschi, T. Saha-Dasgupta, O. K. Andersen, G. Sangiovanni, K. Held, and M. Marsi, Nature Communications **1**, 105 (2010).

[36] A. Okamoto, Y. Fujita, and C. Tatsuyama, Journal of the Physical Society of Japan **52**, 312 (1983), https://doi.org/10.1143/JPSJ.52.312.

[37] Y. Tian, A. A. Reijnders, G. B. Osterhoudt, I. Valmianski, J. G. Ramirez, C. Urban, R. Zhong, J. Schneeloch, G. Gu, I. Henslee, and K. S. Burch, Review of Scientific Instruments **87**, 043105 (2016), https://doi.org/10.1063/1.4944559.

[38] W. Cochran, Phys. Rev. Lett. **3**, 412 (1959).

[39] U. Bismayer, "10. hard mode spectroscopy of phase transitions," in *Transformation Processes in Minerals*, edited by S. A. Redfern and M. A. Carpenter (De Gruyter, 2018) pp. 265–284.

[40] F. A. Chudnovskii, V. N. Andreev, V. S. Kuksenko, V. A. Piculin, D. I. Frolov, P. A. Metcalf, and J. M. Honig, Journal of Solid State Chemistry France **133**, 430 (1997).

[41] X.-B. Chen, M.-H. Kong, J.-Y. Choi, and H.-T. Kim, Journal of Physics D: Applied Physics **49**, 465304 (2016).

[42] W. Bao, C. Broholm, G. Aeppli, P. Dai, J. M. Honig, and P. Metcalf, Phys. Rev. Lett. **78**, 507 (1997).